Photonic Signatures of Spin-Driven Ferroelectricity in Multiferroic Dielectric Oxides

Vakhtang Jandieri,[1] Ramaz Khomeriki,[2] Levan Chotorlishvili,[3,6] Koki Watanabe,[4] Daniel Erni,[1] Douglas H. Werner,[5] and Jamal Berakdar[3]

[1]*General and Theoretical Electrical Engineering (ATE), Faculty of Engineering, University of Duisburg-Essen and CENIDE - Center for Nanointegration Duisburg-Essen, D-47048 Duisburg, Germany*

[2]*Physics Department, Tbilisi State University, 3 Chavchavadze, 0128 Tbilisi, Georgia*

[3]*Institut für Physik, Martin-Luther-Universität, Halle-Wittenberg, D-06099 Halle/Saale, Germany*

[4]*Department of Information and Communication Engineering, Fukuoka Institute of Technology, 3-30-1 Wajirohigashi, Higashi-ku, Fukuoka 811-0295, Japan*

[5]*Department of Electrical Engineering, The Pennsylvania State University, University Park, Pennsylvania 16802, USA*

[6]*Department of Physics and Medical Engineering, Rzeszow University of Technology, 35-959 Rzeszow, Poland*

(Received 10 March 2021; accepted 17 August 2021; published 17 September 2021)

We study the dispersion and scattering properties of electromagnetic modes coupled to a helically ordered spin lattice hosted by a dielectric oxide with a ferroelectric polarization driven by vector spin chirality. Quasianalytical approaches and full-fledged numerics evidence the formation of a chiral magnonic photonic band gap and the presence of gate-voltage dependent circular dichroism in the scattering of electromagnetic waves from the lattice. Gating couples to the emergent ferroelectric polarization and hence, to the underlying vector-spin chirality. The theory relies on solving simultaneously Maxwell's equations coupled to the driven localized spins taking into account their spatial topology and spatial anisotropic interactions. The developed approach is applicable to various settings involving noncollinear spins and multiferroic systems with potential applications in noncollinear magnetophotonics.

DOI: 10.1103/PhysRevLett.127.127601

Introduction.—Photonic material engineering enables precise control of electromagnetic (EM)-field characteristics, including dispersion, propagation, and polarization properties [1]. Structuring dielectrics into waveguides, gratings, photonic crystals, photonic textures with metallic (plasmonic) inclusions in various nontrivial topologies [2,3], or using magnetic metamaterials (albeit to a lesser extent due to smaller coupling of EM fields with spins [4,5]) has led to important findings with technological implications [7]. In this context, oxides, particularly those with ferroelectric ordering are gaining increased attention for photonic applications [8] by offering multifunctionality via external parameters (gating via electric and/or by applying magnetic near fields) that modify the optical response.

In this Letter, we focus on magnetophotonics in dielectric multiferroic oxide with magnetically induced ferroelectricity. Particularly , interesting are oxides with a helical ordering of spins $\mathbf{S_j}$ ($\mathbf{j}$ is a lattice position vector) which has been traced to spin-orbit coupling, electronic correlations, and crystal field effects [9]. The vector spin chirality $\mathbf{S_j} \times \mathbf{S_{j+1}}$ is an even function under time reversal but odd under spatial inversion signaling a possible emergence of ferroelectric polarization [10,11] and hence a magnetoelectric coupling; examples of such multiferroic materials are RMn_2O_5 (R = Y,Ho,Bi) [12], $DyMnO_3$ [13], or $TbMnO_3$ for which magnetic responses have been observed via THz radiation [14]. The interrelation between polarization and vector-spin chirality allows controlling the latter via a static electric field, e.g., via a gate voltage. Thus, photonic effects related to the helical order can also be voltage controlled. We develop a scheme for treating the scattering of EM waves in the helical spin lattice using Maxwell equations coupled to the dynamics of spin excitations in the linear regime.

We calculate the spectral characteristics of the band gap regions from a simplified analytical model as well as from a full-wave scheme based on the rigorous coupled-wave method (RCWM). Our approach is applicable to dielectrics with magnetically induced ferroelectricity and is extendable to other multiferroics where ferroelectricity (or its major part) is independent of the magnetic order (e.g., $BiFeO_3$ [15] or GaV_4S_8 [16]). In this case, the intrinsic ferroelectric dynamics should be taken into account.

Fully discretized model of the problem.—Studying the EM-field-driven dynamic of a dielectric with ferroelectricity induced by vector-spin chirality requires solving the equation of motion of the locally ordered spins and EM wave equation in a self-consistent manner. Let $\mathbf{S}_{\ell,m,n}$ be the magnetic moment at the site (ℓ, m, n) in a 3D lattice, where m and n number the spin numbers in the y-z plane, while ℓ refer to the spins along the x direction (see Fig. 1 for the schematics of the 3D spin system). Neighboring spins are coupled via symmetric and antisymmetric exchange

 © 2021 American Physical Society

resulting in the following effective model: The antisymmetric exchange described by the Dzyaloshinskii-Moriya vector $\mathbf{D}$ [17,18] acts along the x direction. The neighboring spins located in adjacent y-z planes are antiferromagnetically coupled (with an exchange constant J_A), and the spins in the y-z plane are ferromagnetically coupled (with an exchange strength J). The helical ordering entails a spin-current (or vector-spin chirality)-driven effective ferroelectric polarization $\mathbf{P}_{\ell,m,n}$ [10,11] that couples to a static electric field $\mathbf{E}_0$. The energy density can be expressed as

$$\mathcal{H} = \sum_{\ell,m,n} \{ -J\mathbf{S}_{\ell,m,n}\mathbf{S}_{\ell,m+1,n} - J\mathbf{S}_{\ell,m,n}\mathbf{S}_{\ell,m,n+1} + \mathbf{D}\cdot[\mathbf{S}_{\ell,m,n}\times\mathbf{S}_{\ell,m+1,n}] + J_A\mathbf{S}_{\ell,m,n}\mathbf{S}_{\ell+1,m,n} + K_2(S^x_{\ell,m,n})^2 - \mathbf{E}_0\mathbf{P}_{\ell,m,n}\} \quad (1)$$

where K_2 is the strength of the magnetic anisotropy in the (y-z) plane [for specific oxides such as $TbMnO_3$, the additional terms related to magnetic anisotropies and variations of the exchange constants should be included in Eq. (1) [19]]. In the setup shown in Fig. 1, $\mathbf{D}$ is directed along the x axis. Moreover, the static electric field is along the z axis. $\mathbf{P}_{\ell,m,n}$ follows from the ordering of the magnetic moments $\mathbf{S}_{\ell,m,n}$ as [10,11]

$$\mathbf{P}_{\ell,m,n} = g_{\mathrm{em}}\{\mathbf{e}\times[\mathbf{S}_{\ell,m,n}\times\mathbf{S}_{\ell,\mathbf{m}',\mathbf{n}'}]\} \quad (2)$$

where g_{em} is the magnetoelectric coupling constant and $\mathbf{e}$ is the unit vector connecting the nearest ℓ, m, n and ℓ, m', n' spins. The spins along the x (z) axis are antiferromagnetically (ferromagnetically) aligned. The ordering along the y direction follows from the energy functional [as a consequence of Eq. (2)]:

$$\sum_m -J\mathbf{S}_m\mathbf{S}_{m+1} + K_2(S^z_m)^2 + D'(S^x_m S^y_{m+1} - S^y_m S^x_{m+1}),$$

where the indexes n and ℓ are suppressed, and $D' \equiv |\mathbf{D}| - g_{\mathrm{em}}|\mathbf{E}_0|$ is an effective Dzyaloshinskii-Moriya vector constant. For $TbMnO_3$ the remnant helicity index is $Q_0 \simeq 0.28/a$, where a is an intralayer lattice constant. With an applied static electric field $\mathbf{E}_0$ (along z) one can decrease the helicity index, thus smoothing the noncollinear ordering. Indeed, a minimization of the energy functional yields a helical structure with the helicity index Q defined as $\tan(aQ) = D'/aJ$, and an associated helical ground state with a helical period $w = 2\pi/Q$ (cf. Fig. 1) is given in the following form:

$$\mathbf{S}^{0x}_{\ell,m,n} = 0, \qquad \mathbf{S}^{0y}_{\ell,m,n} + i\mathbf{S}^{0z}_{\ell,m,n} = S_0 e^{iQam}(-1)^{\ell}. \quad (3)$$

The dynamics of an incoming electromagnetic wave coupled to the local magnetic response is governed by the following expressions:

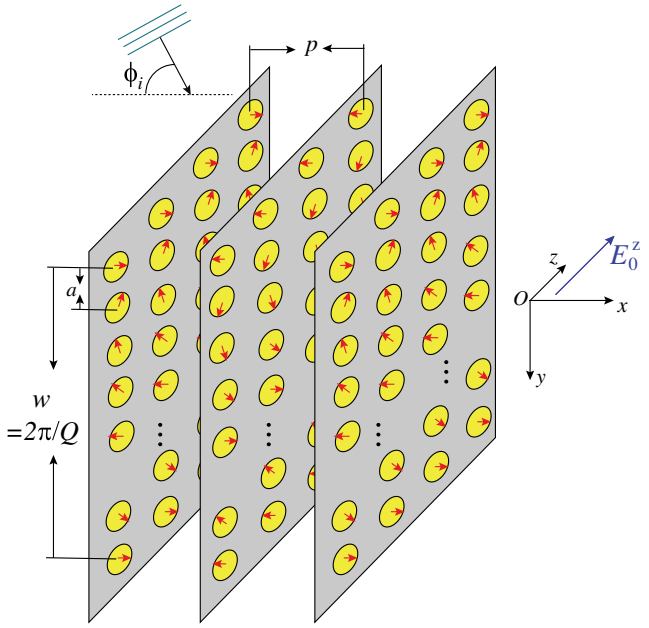

FIG. 1. Schematic of the considered sample with a spin-current-driven helical spin order in the y-z plane and an antiferromagnetic ordering along the x axis. A spin-driven ferroelectric polarization along the z axis couples to an applied static electric field E_0^z (caused by a gate voltage). The lattice spacing in the y-z planes is a, and p is an interlayer spacing. The helical period $w = 2\pi/Q$ is set by the helicity index Q (or y component of the spin chirality vector). Plane waves are impinging from free space with an angle of incidence ϕ_i.

$$\frac{d\mathbf{S}_{\ell,m,n}}{dt} = |\gamma|\mu_0[\mathbf{S}_{\ell,m,n}\times\mathbf{H}_{\ell,m,n}],$$
$$\frac{1}{c^2}\frac{\partial^2}{\partial t^2}[\mathbf{H}+\mathbf{S}]_{\ell,m,n} = [\Delta\mathbf{H} - \nabla(\nabla\cdot\mathbf{H})]_{\ell,m,n}, \quad (4)$$

where $\mathbf{H}$ is the magnetic-field vector component of the EM wave and γ is the gyromagnetic ratio. In Eq. (4) the interaction of the EM wave with the polarization vector [Eq. (2)] has been neglected because of the small value of the magnetoelectric coupling constant g_{em}. Only the coupling of the electric polarization with the external static electric field $\mathbf{E}_0$ is taken into account, which allows control over the helicity index of the resulting ground state Eq. (3). In the case of multiferroics [15,16] with an intrinsic electric polarization the coupling to the $\mathbf{E}$-field component of the traversing EM wave should be taken into account and, moreover, the evolution equation for the polarization vector should be considered [20,21]:

$$\mu_0\frac{\partial}{\partial t}[\mathbf{H}+\mathbf{S}] = -\nabla\times\mathbf{E}, \quad \frac{\partial}{\partial t}[\epsilon_0\mathbf{E}+\mathbf{P}] = \nabla\times\mathbf{H}$$
$$\frac{d\mathbf{S}}{dt} = |\gamma|\mu_0[\mathbf{S}\times\mathbf{H}], \quad \frac{d^2\mathbf{P}}{dt^2} = -\omega_P^2[\mathbf{P}-\chi(0)\mathbf{E}], \quad (5)$$

where μ_0 and ϵ_0 are the permeability and permittivity of free space, respectively, ω_P is the ferroelectric resonance frequency, and $\chi(0)$ is an electric susceptibility at the zero mode frequency [indexes in Eq. (5) are suppressed]. The analysis procedure of Eq. (5) is similar to that described below, but here, we only consider evaluating Eq. (4) both analytically and numerically. Linearizing Eq. (4) with respect to the ground state Eq. (3), we obtain the following system of equations:

$$\left(\frac{\omega^2}{c^2}-F_b\right)h^y_{\mathbf{k}}-N_{ab}h^x_{\mathbf{k}}+\frac{\omega_M\omega}{2c^2}(h^x_{\mathbf{k+Q}}-h^x_{\mathbf{k-Q}})=0; \qquad \left(\frac{\omega^2}{c^2}-F_b-F_a\right)h^z_{\mathbf{k}}+i\frac{\omega_M\omega}{2c^2}(h^x_{\mathbf{k+Q}}+h^x_{\mathbf{k-Q}})=0;$$
$$\left(\frac{\omega^2}{c^2}-F_a\right)h^x_{\mathbf{k}}-N_{ab}h^y_{\mathbf{k}}-\frac{\omega_M\omega}{2c^2}(h^y_{\mathbf{k+Q}}-h^y_{\mathbf{k-Q}}+ih^z_{\mathbf{k+Q}}+ih^z_{\mathbf{k-Q}})=0, \tag{6}$$

where $\mathbf{h}\equiv\mathbf{H}/S_0$, $h^\nu_{\mathbf{k}}$ is the νth component of the magnetic field for the mode with the wave vector $\mathbf{k}$ ($\mathbf{k}\equiv(k_x,k_y,k_z=0)$), $F_a=2(1-\cos k_y a)/a^2$, $F_b=2(1-\cos k_x p)/p^2$, $N_{ab}=(e^{ik_x p}-1)(e^{ik_y a}-1)/(ap)$, $\mathbf{Q}\equiv(\pi/p,Q,0)$ is the periodicity vector of the helical lattice, $\omega_M=|\gamma|\mu_0 S_0$ (which is in the THz range [14]), and p is the interlayer spacing.

For approximate analytical expressions of the mode dispersion within the frequency range of the first band gap, we allow in Eq. (6) three modes with wave vectors: $\mathbf{k}$, $\mathbf{k}-\mathbf{Q}$, and $\mathbf{k}-\mathbf{2Q}$. In the limit $k_x p\ll 1$ (interlayer spacing p is much smaller than the excitation wavelength along the x axis), the modes with $\mathbf{k}$ and $\mathbf{k}-\mathbf{2Q}$ couple around their crossing point at $k_y=Q$. Unlike 1D periodic structures [22,23], where the band gap regions appear at $\mathrm{Re}\{k_y\}/Q_{1d}=0.5,1.0,1.5,\ldots$ (Q_{1d} is the 1D structure periodicity), the effective helical index of our lattice is $2Q$. The first band gap emerges at $\mathrm{Re}\{k_y\}/Q=1.0$ (cf. Fig. 2). The mode associated with $\mathbf{k}-\mathbf{Q}$ is well separated from the region $k_y=Q$ and from the branches of dispersion of the other two modes. The magnetic-field components for the $\mathbf{k}-\mathbf{Q}$ mode around the crossing point are $h^y_{\mathbf{k-Q}}=h^z_{\mathbf{k-Q}}=0$, $h^x_{\mathbf{k-Q}}=\omega_M/2\omega(h^y_{\mathbf{k}}-h^y_{\mathbf{k-2Q}}+ih^z_{\mathbf{k}}+ih^z_{\mathbf{k-2Q}})$. Equation (6) can be rewritten in the compact form $\tilde{\mathbf{A}}\cdot\mathbf{g}=0$, where $\tilde{\mathbf{A}}$ is expressed in the following form:

$$\tilde{\mathbf{A}}=\begin{bmatrix}
\frac{\omega^2}{c^2}-k_x^2 & 0 & k_xk_y & \frac{\omega_M^2}{4c^2} & -i\frac{\omega_M^2}{4c^2} & 0\\
0 & \frac{\omega^2}{c^2}-k_x^2-k_y^2 & 0 & -i\frac{\omega_M^2}{4c^2} & -\frac{\omega_M^2}{4c^2} & 0\\
k_xk_y & 0 & \frac{\omega^2}{c^2}-k_y^2 & 0 & 0 & 0\\
\frac{\omega_M^2}{4c^2} & i\frac{\omega_M^2}{4c^2} & 0 & \frac{\omega^2}{c^2}-k_x^2 & 0 & k_x(k_y-2Q)\\
i\frac{\omega_M^2}{4c^2} & -\frac{\omega_M^2}{4c^2} & 0 & 0 & \frac{\omega^2}{c^2}-k_x^2-(k_y-2Q)^2 & 0\\
0 & 0 & 0 & k_x(k_y-2Q) & 0 & \frac{\omega^2}{c^2}-(k_y-2Q)^2
\end{bmatrix}$$

and $\mathbf{g}=(h^y_{\mathbf{k}},h^z_{\mathbf{k}},h^x_{\mathbf{k}},h^y_{\mathbf{k-2Q}},h^z_{\mathbf{k-2Q}},h^z_{\mathbf{k-2Q}})^T$ (T means transpose). Equating the determinant of matrix $\tilde{\mathbf{A}}$ to zero, an analytical expression characterizing the dispersion of two Bloch modes is obtained. Based on the derived expression, we estimate the angular frequency ω_P at which the band gap region is located at:

$$\omega_P\simeq cQ/\sin(\phi_i). \tag{7}$$

We deduce also approximate expressions for the real and imaginary parts of the transverse wave number k_y as a function of the angular frequency ω and the angle of incidence ϕ_i. The imaginary part of k_y for the first mode exhibits a sharp peak around ω_P (cf. solid line in Fig. 2). The peak value $G\equiv[\mathrm{Im}(k_y)]^{max}$ is set by

$$G(\phi_i)=\frac{\omega_M^2}{4c^2Q}\frac{2-\sin^2(\phi_i)}{2}. \tag{8}$$

and the peak width is given as $\Lambda=cG(\phi_i)/[2\sin(\phi_i)]$.

The transverse wave number k_y for the second mode (dashed line in Fig. 2) is always real, and our sample is transparent to this mode with the magnetic-field components: $h^x_{\mathbf{k}}=A$, $h^y_{\mathbf{k}}=-A\cot(\phi_i)$, and $h^z_{\mathbf{k}}=-iA\cot(\phi_i)$, where A is the amplitude of the magnetic field. With these findings we conclude that the mode is expressible as a superposition of TE and TM waves. Assuming that the

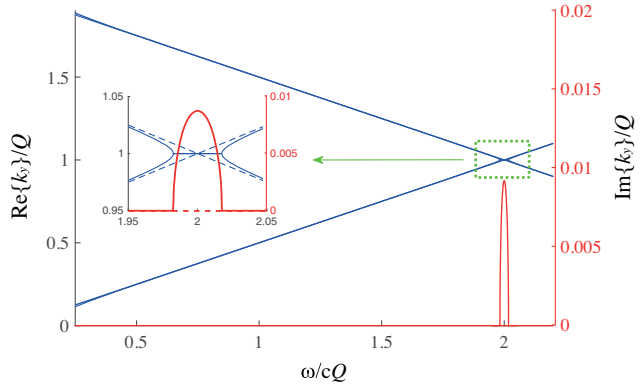

FIG. 2. Real (blue) and imaginary (red) parts of k_y/Q for two Bloch modes (solid and dashed lines) versus the normalized frequency $\omega/(cQ)$ at $\phi_i = 30°$. The inset shows an enlarged view of the band gap region.

reflection of the lattice is given as $\mathcal{R} = \mathrm{Im}(k_y)d_y$, where d_y is the thickness of the sample along the y axis, the approximate peak values of both TE and TM waves can be written as follows:

$$\mathcal{R}_{\mathrm{TM}}^{\max} \sim d_y Q, \qquad \mathcal{R}_{\mathrm{TE}}^{\max} = -i\cos(\phi_i)\mathcal{R}_{\mathrm{TM}}^{\max}. \tag{9}$$

Using the same arguments we can deduce the ratio between the right and left circularly polarized EM wave's reflectivity peaks $R_R^{\max}/R_L^{\max} = \sin(\phi_i)$ and conclude the existence of a circular dichroism for a specific helical order characterized by $\mathbf{Q}$. Inverting the chirality of the helix changes the sign of the circular dichroism. The chirality inversion can be realized by changing the magnitude of the applied field $\mathbf{E}_0$. In the collinear case ($\mathbf{Q} = 0$) linear dichroism persists for much larger frequencies than considered here, due to the antiferromagnetic interlayer ordering and the ferromagnetic intralayer ordering.

Rigorous coupled-wave method.—To go beyond approximate models that yielded explicit expressions for the bound and stop band regions, we apply a RCWM [24] to our system (Fig. 1). The RCWM can efficiently analyze arbitrary gratings of anisotropic materials. A relation between the spin magnetization density $\mathbf{S}(x, y)$ and the magnetic field $\mathbf{H}(x, y)$ in the grating layer is expressed through the permeability tensor $\bar{\bar{\mu}}(x)$ in the following form:

$$\mathbf{S}(x,y) = \mu_0 \begin{pmatrix} 0 & i\mu_1(x) & -i\mu_2(x) \\ -i\mu_1(x) & 0 & 0 \\ i\mu_2(x) & 0 & 0 \end{pmatrix} \mathbf{H}(x,y). \tag{10}$$

The local and frequency dependent elements of the permeability tensor read $\mu_1(x) = (\omega_M/\omega)\cos(\pi x/p)$ and $\mu_2(x) = (\omega_M/\omega)\sin(\pi x/p)$. As in the previous section, the initial expressions for RCWM are Eq. (4), which guarantees that both approaches are consistent. The x, y, and z components of the electromagnetic fields are pseudoperiodic functions of x with a period $2p$ and can be approximately expanded into a truncated Fourier series in the following form:

$$\begin{bmatrix} \mathbf{E}(x,y) \\ \mathbf{H}(x,y) \end{bmatrix} = \sum_{n=-N}^{N} \begin{bmatrix} \mathbf{e}_n(y) \\ \mathbf{h}_n(y) \end{bmatrix} e^{i(k_x + \pi n/p)x}, \tag{11}$$

where $k_x = (\omega/c)\cos(\phi_i)$ and N is a truncation number associated with the Fourier series. The truncation number N is taken as 5 to satisfy the principle of conservation of energy. Expressing the y component of the electric and magnetic fields through the x and z components, Maxwell's equations can be transformed into the following coupled differential equations:

$$\frac{\partial}{\partial y}\begin{bmatrix} e_x \\ e_z \\ h_x \\ h_z \end{bmatrix} = ik_0\bar{\bar{\mathbf{U}}}\begin{bmatrix} e_x \\ e_z \\ h_x \\ h_z \end{bmatrix} = ik_0\begin{bmatrix} 0 & 0 & \mathbf{U}_{13} & \mathbf{U}_{14} \\ 0 & \mathbf{U}_{22} & \mathbf{U}_{23} & \mathbf{U}_{24} \\ 0 & \mathbf{U}_{32} & \mathbf{U}_{33} & 0 \\ \mathbf{U}_{41} & 0 & 0 & 0 \end{bmatrix}\begin{bmatrix} e_x \\ e_z \\ h_x \\ h_z \end{bmatrix}$$

where

$$\mathbf{U}_{13} = -i[\![\mu_2]\!], \qquad \mathbf{U}_{14} = -\mathbf{I} + \mathbf{K}^2 \tag{12}$$

$$\mathbf{U}_{22} = -i[\![\mu_1]\!]\mathbf{K}, \quad \mathbf{U}_{23} = \mathbf{I} - [\![\mu_1]\!]^2, \quad \mathbf{U}_{24} = -i[\![\mu_2]\!] \tag{13}$$

$$\mathbf{U}_{32} = \mathbf{I} - \mathbf{K}^2, \qquad \mathbf{U}_{33} = i\mathbf{K}[\![\mu_1]\!], \qquad \mathbf{U}_{41} = -\mathbf{I} \tag{14}$$

with

$$([\![\Upsilon]\!])_{n,m} = \frac{1}{2p}\int_0^{2p} \Upsilon(x)e^{-i(n-m)\pi x/p}dx, \qquad \Upsilon = [\mu_1, \mu_2] \tag{15}$$

$$(\mathbf{K})_{n,m} = \delta_{n,m}\left(\frac{k_x}{k_0} + \frac{\pi n}{pk_0}\right). \tag{16}$$

Here k_0 is the free-space wave number, $[\![\Upsilon]\!]$ is a square Toeplitz matrix generated by the Fourier coefficients of Υ with the (n, m) entries equal to Υ_{n-m}, $\bar{\bar{\mathbf{U}}}$ is a $(8N + 4) \times (8N + 4)$ square matrix, $\mathbf{I}$ is the unit matrix, and $\delta_{n,m}$ is the Kronecker's delta function. Multiple scattering between anisotropic layers is described by solving for the scattering S matrix which yields the relation between the incoming and outgoing wave amplitudes [25–27]. The reflection and transmission matrices for each anisotropic layer are

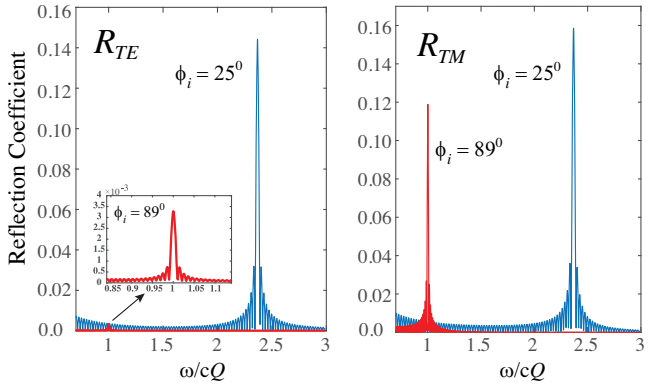

FIG. 3. Dependence of the amplitudes of the reflected fields R_{TE} (for TE polarization) and R_{TM} (for TM polarization) versus $\omega/(cQ)$ at two angles of incidence for waves impinging on the helical lattice from free space: $\phi_i = 25°$ (blue line) and $\phi_i = 89°$ (red line). The thickness of the sample is $d_y = 50w$, $a = 2p$, and $\omega_M/(2cQ) = 0.04$. The results are calculated using a full-wave numerical analysis based on RCWM.

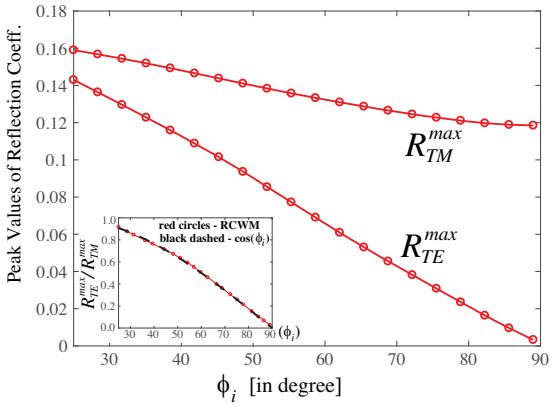

FIG. 4. Numerical results for the peak values of the reflection coefficients for both TE and TM polarizations versus the angle of incidence ϕ_i. Inset: the ratio $R_{\mathrm{TE}}^{\max}/R_{\mathrm{TM}}^{\max}$ (red circles) compared with Eq. (8) (black dotted line).

expressed through the eigenvectors and eigenvalues of $\bar{\bar{\mathbf{U}}}$, whose components are given in Eqs. (11)–(13). Since the reflection and transmission matrices for each layer are defined, the generalized reflection matrix viewed from the outermost region (region of incident wave) is calculated using a recursive algorithm starting from the lowermost region [25–27].

Dependence of the amplitudes of the reflected fields R_{TE} (TE polarization) and R_{TM} (TM polarization) versus $\omega/(cQ)$ at two angles of the incident wave, namely at $\phi_i = 25°$ (blue line) and $\phi_i = 89°$ (red line), are illustrated in Fig. 3, respectively. The thickness of the sample is taken as $d_y = 50w$, $a = 2p$, a helical step angle along the y axis that is equal to 36° (i.e., ten rotations within one period of w) and $\omega_M/(2cQ) = 0.04$. An enlarged figure of the reflection peak at $\phi_i = 89°$ for TE polarization is also shown as an inset. Firstly, from both figures it follows that narrow bandgap regions are formed exactly at the same frequencies as given analytically in Eq. (6). Next, we note that the amplitude of the reflected field for TE polarization is approaching zero in proportion to the angle of incidence, whereas this is not the case for TM wave incidence. This is in agreement with Eq. (8), where the reflection peak for TE polarization is proportional to $\cos(\phi_i)$. The dependence of the peak values of the reflection coefficients for both polarizations—$R_{\mathrm{TE}}^{\max}$ and $R_{\mathrm{TM}}^{\max}$—versus the angle of incidence ϕ_i obtained using RCWM is demonstrated in Fig. 4. The ratio $R_{\mathrm{TE}}^{\max}/R_{\mathrm{TM}}^{\max}$ is shown as an inset by the red line and compared with that obtained using Eq. (8) demonstrated by the black dotted line [note that the latter is equal to $\cos(\phi_i)$]. Very good agreement is observed between the results obtained based on both approaches. The approximate analytical approach—a fully discretized model—captures very well the positions of the peaks as well as the widths and ratios of the reflection coefficients' peaks (cf. inset in Fig. 4). However, it fails to predict the absolute values of the reflected fields for each polarization separately.

Conclusions.—The coupling of EM waves with helically ordered spin lattice with emergent ferroelectric polarization was studied. The formation of helical spin-photonic band gaps is analyzed theoretically and numerically. Expressions for band locations and widths are analytically derived and confirmed with full-fledged numerics. The method is extendable to encompass synthetic antiferromagnets [28] including Dzyaloshinskii-Moriya interactions, or ordered multiferroic tunnel junctions [29] pointing to the potential of chiral magnetophotonics.

This work is supported in part by the Grant No. FR-19-4049 from Shota Rustaveli National Science Foundation of Georgia and the DFG through SFB-TRR227.

[1] E. Yablonovitch, Inhibited Spontaneous Emission in Solid-State Physics and Electronics, Phys. Rev. Lett. **58**, 2059 (1987); S. John, Strong Localization of Photons in Certain Disordered Dielectric Superlattices, Phys. Rev. Lett. **58**, 2486 (1987); J. D. Joannopoulos, S. G. Johnson, J. N. Winn, and R. D. Meade, *Photonic Crystals: Molding the Flow of Light* (Princeton University Press, Princeton, 2008).

[2] M. Hafezi, E. Demler, M. Lukin, and J. Taylor, Robust optical delay lines with topological protection, Nat. Phys. **7**, 907 (2011); J. Noh, S. Huang, D. Leykam, Y. Chong, K. Chen, and M. Rechtsman, Experimental observation of optical Weyl points and Fermi arc-like surface states, Nat. Phys. **13**, 611 (2017); M. Rechtsman, J. Zeuner, Y. Plotnik, Y. Lumer, D. Podolsky, F. Dreisow, S. Nolte, M. Segev, and A. Szameit, Photonic Floquet topological insulators, Nature (London) **496**, 196 (2013).

[3] Z. Wang, Y. Chong, J. Joannopoulos, and M. Soljai, Observation of unidirectional backscattering-immune

topological electromagnetic states, Nature (London) **461**, 772 (2009).

[4] A. G. Gurevich and G. A. Melkov, *Magnetization Oscillations and Waves* (CRC Press, New York, 1996).

[5] Driving magnetism with intense lasers is an active field of research [6] but outside of scope here.

[6] A. V. Kimel, A. Kirilyuk, P. A. Usachev, R. V. Pisarev, A. M. Balbashov, and Th. Rasing, Ultrafast non-thermal control of magnetization by instantaneous photomagnetic pulses, Nature (London) **435**, 655 (2005); F. Cheng, Z. Du, X. Wang, Z. Cai, L. Li, C. Wang, A. Benabbas, P. Champion, N. Sun, L. Pan, and Y. Liu, All-optical helicity-dependent switching in hybrid metal-ferromagnet thin films, Adv. Opt. Mater. **8**, 2000379 (2020).

[7] N. Engheta and R. W. Ziolkowski, *Metamaterials: Physics and Engineering Explorations* (Wiley-IEEE Press, New York, 2006); S. A. Maier, *Plasmonics: Fundamentals and Applications* (Spinger, New York, 2007).

[8] C. Xiong, W. H. P. Pernice, J. H. Ngai, J. W. Reiner, D. Kumah, F. J. Walker, C. H. Ahn, and H. X. Tang, Active silicon integrated nanophotonics: Ferroelectric $BaTiO_3$ devices, Nano Lett. **14**, 1419 (2014); J. E. Ortmann, A. Y. Borisevich, S. Kwon, A. Posadas, M. J. Kim, and A. A. Demkov, Three-dimensional integration of functional oxides and crystalline silicon for optical neuromorphic computing using nanometer-scale oxygen scavenging barriers, ACS Appl. Nano Mater. **4**, 2153 (2021); J. E. Ortmann, M. R. McCartney, A. Posadas, D. J. Smith, and A. A. Demkov, Epitaxial oxides on glass: A platform for integrated oxide devices, ACS Appl. Nano Mater. **2**, 7713 (2019); T. Jin, L. Li, B. Zhang, Hao-Yu G. Lin, H. Wang, and P. T. Lin, Monolithic mid-infrared integrated photonics using silicon-on-epitaxial barium titanate thin films, ACS Appl. Mater. Interfaces **9**, 21848 (2017); F. Eltes, D. Caimi, F. Fallegger, M. Sousa, E. OConnor, M. D. Rossell, B. Offrein, J. Fompeyrine, and S. Abel, Low-loss $BaTiO_3Si$ waveguides for nonlinear integrated photonics, ACS Photonics **3**, 1698 (2016); A. Karvounis, F. Timpu, V. V. VoglerNeuling, R. Savo, and R. Grange, Barium titanate nanostructures and thin films for photonics, Adv. Opt. Mater. **8**, 2001249 (2020); A. Karvounis, V. V. VoglerNeuling, F. U. Richter, E. Dnervaud, M. Timofeeva, and R. Grange, Electrooptic metasurfaces based on barium titanate nanoparticle films, Adv. Opt. Mater. **8**, 2000623 (2020); M. Duncan, J. E. Ortmann, and A. A. Demkov, Dynamic waveguiding in silicon-integrated barium titanate thin films, in *Proceedings of the 2019 IEEE MTT-S International Conference on Numerical Electromagnetic and Multiphysics Modeling and Optimization (NEMO)* (IEEE, Boston, 2019), https://ieeexplore.ieee.org/abstract/document/8853782; S. Abel, F. Eltes, J. E. Ortmann, A. Messner, P. Castera, T. Wagner, D. Urbonas, A. Rosa, A. M. Gutierrez, D. Tulli, P. Ma, B. Baeuerle, A. Josten, W. Heni, D. Caimi, L. Czornomaz, A. A. Demkov, J. Leuthold, P. Sanchis, and J. Fompeyrine, Large pockels effect in micro- and nanostructured barium titanate integrated on silicon, Nat. Mater. **18**, 42 (2019); S. Bogdanov, M. Y. Shalaginov, A. Boltasseva, and V. M. Shalaev, Material platforms for integrated quantum photonics, Opt. Mater. Express **7**, 111 (2017).

[9] M. Fiebig, Th. Lottermoser, D. Meier, and M. Trassin, The evolution of multiferroics, Nat. Rev. Mater. **1**, 16046 (2016).

[10] H. Katsura, N. Nagaosa, and A. V. Balatsky, Spin Current and Magnetoelectric Effect in Noncollinear Magnets, Phys. Rev. Lett. **95**, 057205 (2005).

[11] M. Mostovoy, Ferroelectricity in Spiral Magnets, Phys. Rev. Lett. **96**, 067601 (2006).

[12] S.-W. Cheong and M. Mostovoy, Multiferroics: A magnetic twist for ferroelectricity, Nat. Mater. **6**, 13 (2007); C. Vecchini, L. C. Chapon, P. J. Brown, T. Chatterji, S. Park, S.-W. Cheong, and P. G. Radaelli, Commensurate magnetic structures of RMn_2O_5 (R = Y,Ho,Bi) determined by single-crystal neutron diffraction, Phys. Rev. B, **77**, 134434 (2008).

[13] F. Kagawa, M. Mochizuki1 Y. Onose, H. Murakawa, Y. Kaneko, N. Furukawa, and Y. Tokura, Dynamics of Multiferroic Domain Wall in Spin-Cycloidal Ferroelectric $DyMnO_3$, Phys. Rev. Lett. **102**, 057604 (2009).

[14] T. Kubacka *et al.*, Large-amplitude spin dynamics driven by a THz pulse in resonance with an electromagnon, Science **343**, 1333 (2014).

[15] J. Wang, J. B. Neaton, H. Zheng, V. Nagarajan, S. B. Ogale, B. Liu, D. Viehland, V. Vaithyanathan, D. G. Schlom, U. V. Waghmare, N. A. Spaldin, K. M. Rabe, M. Wuttig, and R. Ramesh, Epitaxial $BiFeO_3$ multiferroic thin film heterostructures, Science **299**, 1719 (2003).

[16] E. Ruff, S. Widmann, P. Lunkenheimer, V. Tsurkan, S. Bordcs, I. Kzsmrki, and A. Loidl, Multiferroicity and skyrmions carrying electric polarization in GaV_4S_8, Sci. Adv. **1**, e1500916 (2015).

[17] I. Dzyaloshinskii, A thermodynamic theory of weak ferromagnetism of antiferromagnetics, J. Phys. Chem. Solids **4**, 241 (1958).

[18] T. Moriya, Anisotropic superexchange interaction and weak ferromagnetism, Phys. Rev. **120**, 91 (1960).

[19] M. Matsubara, S. Manz, M. Mochizuki, T. Kubacka, A. Iyama, N. Aliouane, T. Kimura, S. Johnson, D. Meier, and M. Fiebig, Magnetoelectric domain control in multiferroic $TbMnO_3$, Science **348**, 1112 (2015).

[20] R. Khomeriki, L. Chotorlishvili, I. Tralle, and J. Berakdar, Positive negative birefringence in multiferroic layered metasurfaces, Nano Lett. **16**, 7290 (2016).

[21] L. Chotorlishvili, R. Khomeriki, A. Sukhov, S. Ruffo, and J. Berakdar, Dynamics of Localized Modes in a Composite Multiferroic Chain, Phys. Rev. Lett. **111**, 117202 (2013).

[22] R. Dreher and G. Meier, Light propagation in helicoidal structures, Solid State Commun. **13**, 607 (1973).

[23] O. V. Ivanov and D. I. Sementsov, Magneto-optical interaction of light with a periodic bi-gyrotropic structure, Pure Appl. Opt. **6**, 455 (1997).

[24] K. Watanabe, Numerical integration schemes used on differential theory for anisotropic gratings, J. Opt. Soc. Am. A **19**, 2245 (2002).

[25] V. Jandieri, P. Baccarelli, G. Valerio, and G. Schettini, 1-D periodic lattice sums for complex and leaky waves in 2-D structures using higher-order Ewald formulation, IEEE Trans. Antennas Propag. **67**, 2364 (2019).

[26] V. Jandieri and K. Yasumoto, Electromagnetic scattering by layered cylindrical arrays of circular rods, IEEE Trans. Antennas Propag. **59**, 2437 (2011).

[27] K. Yasumoto, *Electromagnetic Theory and Applications for Photonic Crystals* (CRC Press, Boca Raton, FL, 2005).

[28] R. A. Duine, K.-J. Lee, S. S. P. Parkin, and M. D. Stiles, Synthetic antiferromagnetic spintronics, Nat. Phys. **14**, 217 (2018).

[29] Y. W. Yin *et al.*, Multiferroic tunnel junctions and ferroelectric control of magnetic state at interface, J. Appl. Phys. **117**, 172601 (2015).